

## ORIGINAL ARTICLE

# Production and Characterization of Dimeric Spike Truncated-nodavirus Capsid Displaying the Receptor-binding Domain of Severe Acute Respiratory Syndrome Coronavirus-2

Ming Hao Chan<sup>1</sup>, Jia Xian Lee<sup>1</sup>, Wen Siang Tan<sup>2</sup>, Mariatulqabtiah Abdul Razak<sup>3,4</sup>, Kok Lian Ho<sup>1</sup>

<sup>1</sup> Department of Pathology, Faculty of Medicine and Health Sciences, Universiti Putra Malaysia, 43400 UPM Serdang, Selangor, Malaysia

<sup>2</sup> Department of Microbiology, Faculty of Biotechnology and Biomolecular Sciences, Universiti Putra Malaysia, 43400 UPM Serdang, Selangor, Malaysia.

<sup>3</sup> Department of Cell and Molecular Biology, Faculty of Biotechnology and Biomolecular Sciences, Universiti Putra Malaysia, 43400 UPM Serdang, Selangor, Malaysia.

<sup>4</sup> Laboratory of Vaccine and Biomolecules, Institute of Bioscience, Universiti Putra Malaysia, 43400 UPM Serdang, Selangor, Malaysia.

## ABSTRACT

**Introduction:** The Covid-19 pandemic has highlighted the essential role of vaccination, even with the availability of antiviral therapies. Although vaccines based on technologies such as mRNA, attenuated viruses, protein subunits, and adenoviral vectors have been granted emergency use approval, issues related to safety, efficacy, and production costs still exist, prompting the need for new, cost-effective, safer, and more efficient vaccine alternatives. This research focuses on evaluating the robustness of virus-like particles (VLPs) derived from the protruding domain truncated capsid protein of *Macrobrachium rosenbergii* nodavirus (CΔ116-MrNV-CP) fused with the receptor-binding domain (RBD) of SARS-CoV-2. **Materials and methods:** The RBD of SARS-CoV-2 was genetically linked to the C-terminus of CΔ116-MrNV-CP to create a novel recombinant protein, CΔ116-MrNV-CP<sup>RBD</sup>. The protein was expressed in *Escherichia coli* and purified using cation-exchange chromatography. Structural characterization was performed via scanning transmission electron microscopy (STEM) and dynamic light scattering (DLS), while its antigenicity and immunogenicity were tested using ELISA and in BALB/c mice. **Results:** Biophysical analysis confirmed that CΔ116-MrNV-CP<sup>RBD</sup> assembled into VLPs of approximately 14 nm in diameter. The RBD displayed on the surface of these VLPs was effectively recognized by an anti-RBD monoclonal antibody. Subcutaneous administration of CΔ116-MrNV-CP<sup>RBD</sup> in mice demonstrated its ability to trigger both humoral and cellular immune responses. **Conclusion:** This study successfully engineered a VLP-based platform that presents the SARS-CoV-2 RBD on the surface of VLPs formed by a recombinant protein. The demonstrated antigenicity and immunogenicity in mice suggest that CΔ116-MrNV-CP could serve as a promising platform for developing VLP-based vaccines targeting SARS-CoV-2. *Malaysian Journal of Medicine and Health Sciences* (2024) 20(SUPP11): 41-50. doi:10.47836/mjmh20.s11.7

**Keywords:** *Macrobrachium rosenbergii* nodavirus, Capsid protein, Receptor-binding domain, Severe acute respiratory syndrome coronavirus-2, Virus-like particles

## Corresponding Author:

Kok Lian Ho, PhD  
Email: klho@upm.edu.my  
Tel : +603-9769-2729

## INTRODUCTION

The outbreak of SARS-CoV-2 has led to a global pandemic, with over 6.9 million deaths reported worldwide as of August 2023 (1). SARS-CoV-2, which causes Covid-19, is a novel zoonotic virus from the *Coronaviridae* family, specifically the *Betacoronavirus* genus within the *Orthocoronavirinae* sub-family. Its genome consists of ~29.9 kb of positive-sense single-stranded RNA (+ssRNA), enclosed within a lipid bilayer that features surface spikes or peplomers (2). Like

other coronaviruses, including SARS-CoV and MERS-CoV, SARS-CoV-2 can infect a wide range of species such as humans, livestock, birds, bats, mice, and wild animals. It primarily targets the respiratory system but can also affect the gastrointestinal tract, liver, and central nervous system (3-5). Its transmission typically occurs via airborne droplets from sneezing, coughing, or close contact, with increased risk in crowded or poorly ventilated spaces, even with social distancing in place (6, 7). The incubation period for SARS-CoV-2 infection varies widely, ranging from 6 to 41 days, leading to a spectrum of outcomes from asymptomatic cases to mild, severe, and occasionally fatal symptoms (8, 9).

The SARS-CoV-2 genome encodes four key structural proteins: spike (S) protein, membrane (M) protein,

nucleocapsid (N) protein, and envelope (E) protein. The spike protein is further divided into two subunits: S1 (amino acids 14–685) and S2 (amino acids 686–1273). The S1 subunit contains the receptor-binding domain (RBD, amino acids 319–541), which is essential for the virus's entry into host cells through the angiotensin-converting enzyme 2 (ACE2) receptor (10, 11). Research has shown that the RBD can effectively stimulate the production of neutralizing antibodies in both *in vitro* and *in vivo* settings, making it a prime target for Covid-19 vaccine design (12-15).

Vaccination continues to be the most effective method for managing the Covid-19 pandemic, even with the availability of antiviral treatments like Remdesivir and Paxlovid. Since March 2020, several vaccines have received emergency use authorizations, including mRNA vaccines such as Pfizer-BioNTech's BNT162b2 (16) and Moderna's mRNA-1273 (17), non-replicating viral vector vaccines such as Oxford-AstraZeneca's ChAdOx1 nCoV-19 (18), and inactivated virus vaccines such as Sinovac's CoronaVac and Bharat Biotech's Covaxin (19). While mRNA vaccines offer high efficacy, quick development timelines, and lower manufacturing costs, they face challenges such as instability, inefficient delivery, and the requirement for ultra-cold storage, which are particularly problematic in low-resource countries lacking cold chain infrastructure (20). Adenoviral vector vaccines, though advantageous due to their rapid expression and high efficiency, involve complex production processes and present safety concerns, such as mutational risks and potential reversion to virulence (21, 22). Thus, the need for affordable, safe, and effective vaccines remains critical.

*Macrobrachium rosenbergii* nodavirus (*MtNV*), responsible for white tail disease (WTD) in larval and post-larval stages of the giant freshwater prawn, is a small, icosahedral, non-enveloped virus belonging to the *Nodaviridae* family (23). The *MtNV* capsid is composed of 180 copies of the capsid protein (*MtNV*-CP) (24, 25). Structurally, the CP is divided into two domains: the shell (S) domain, which forms the spherical core of the capsid, and the protruding (P) domain, which creates dimeric, blade-like spikes on the capsid's surface. *MtNV*-CP can be produced in *Escherichia coli* or *Spodoptera frugiperda* (Sf9) cells and has the ability to self-assemble into virus-like particles (VLPs), which are morphologically similar to the native virus, as confirmed by transmission electron microscopy (TEM) (26, 27). These VLPs, which lack any genetic materials, can be engineered to serve as nanocarriers for various biological molecules, such as DNA or RNA (28). Recent

advancements in modifying the full-length *MtNV*-CP have demonstrated its potential as a vaccine platform by enabling the display of foreign epitopes on its chimeric VLPs (29-33). Typically, these epitopes are presented at the C-terminus of *MtNV*-CP, located at the linker connecting the dimeric spikes and the spherical shell of the VLPs. However, this positioning may hinder the full exposure of the epitopes on the VLP surface, limiting their interaction with host immune cells and reducing immune response efficiency.

To improve epitope presentation, the C-terminal region of the *MtNV*-CP, which comprises residues 256-371, was truncated and replaced with the SARS-CoV-2 RBD, resulting in the creation of the recombinant protein  $\Delta$ 116-*MtNV*-CP<sup>RBD</sup>, which was then expressed in *E. coli*. The immunogenicity, immunophenotyping, and cytokine profiles of  $\Delta$ 116-*MtNV*-CP<sup>RBD</sup> were evaluated in BALB/c mice. The results indicated that immunization with these VLPs generates robust innate, humoral, and cellular immune responses, suggesting that this platform holds significant potential for the development of an effective VLP-based vaccine against SARS-CoV-2.

## MATERIALS AND METHODS

### Construction of recombinant plasmid

To produce the P-domain truncated *MtNV* capsid protein ( $\Delta$ 116-*MtNV*-CP, consisting of amino acids 1-255), specific primers were designed to amplify the coding region of the full-length *MtNV* capsid gene from the plasmid pTrcHis-TARNA2 (26) via polymerase chain reaction (PCR). The PCR primers utilized for this experiment are listed in Table 1. Concurrently, the coding sequence of the RBD from the Wuhan strain (isolate 2019-nCoV WHU01, GenBank ID: MN988668.1), ~600 bp in length, was synthesized with *EcoRI* and *HindIII* restriction sites at the 5' and 3' ends, respectively. PCR amplification was performed using Velocity DNA polymerase (0.5 U, 0.5  $\mu$ L), a 0.2 mM dNTPs mix (0.25  $\mu$ L), 5x Hi-Fi reaction buffer (5  $\mu$ L), 10  $\mu$ M forward and reverse primers (0.5  $\mu$ L each), and nuclease-free water (18.25  $\mu$ L). The thermal cycling program included an initial denaturation step at 98°C for 5 minutes, followed by 35 cycles of denaturation at 98°C for 30 seconds, annealing at 61°C for 1 minute, extension at 72°C for 1 minute, and a final extension at 72°C for 10 minutes. After PCR, the amplified product was purified and cloned into the pTrcHis2 TOPO vector. The resulting recombinant plasmid, pTrcHis- $\Delta$ 116-*MtNV*-CP<sup>RBD</sup>, encoding a fusion protein of 478 amino acids, was introduced into *E. coli* BL21 (DE3) competent cells for expression.

**Table 1: PCR primers used in this study**

Primer	Nucleotide sequence 5'- 3'
Forward CΔ116- M $\Delta$ NV-CP	5'-GGGTAAACCATGGCCCTTAACATCAAGATG- GCTAGAGGTAAA-3' (NcoI site is underlined)
Reverse CΔ116- M $\Delta$ NV-CP	5'-TTTTTGAATTCGCCCTTCCTAACTGT- GAAATTTCCACTGGTGT-3' (EcoRI site is underlined)
Forward Wuhan RBD	5'-GACAGCCATGGCCAATA TTACAAACTTGTGCC-3' (NcoI site is underlined)
Reverse Wuhan RBD	5'-CTGAT <u>AAGCTT</u> CTCCACAAACAGTTGCTGGT-3' (HindIII site is underlined)

### Expression and purification of recombinant proteins

Recombinant proteins were expressed according to the protocol established in a previous study (26) with minor modifications. *Escherichia coli* cells containing the recombinant plasmids were cultured overnight in 20 mL of LB broth supplemented with 100 µg/mL ampicillin at 37°C, with shaking at 200 rpm in a shaking incubator (SASTEC, Malaysia). The overnight culture (10 mL) was then transferred into 1 L of fresh LB broth with 100 µg/mL ampicillin and incubated at 37°C with shaking at 200 rpm until the optical density (OD<sub>600</sub>) reached 0.6 to 0.8. Protein expression was induced with 1 mM isopropyl β-D-1-thiogalactopyranoside (IPTG), followed by incubation at 25°C with shaking at 200 rpm for 5 hours. *Escherichia coli* cells were harvested by centrifugation at 8,000 x g for 5 minutes at 4°C. The cell pellets were resuspended in 10 mL HEPES buffer (50 mM HEPES, 100 mM NaCl; pH 7.4; 10 mL) with the addition of MgCl<sub>2</sub> (4 mM), lysozyme (0.2 mg/mL), PMSF (2 mM), DNase 1 (0.02 mg/mL) and Triton X-100 [0.1% (v/v)]. The suspension was incubated at room temperature on a disc rotator (Stuart, UK) for 2 hours and then centrifuged at 18,000 x g for 10 minutes at 4°C. The supernatant was filtered through a 0.22 µm Minisart NML syringe filter (Sartorius, Germany). The filtered crude lysate containing CΔ116-M $\Delta$ NV-CP<sup>RBD</sup> was loaded into a HiTrap SP HP 1 mL column (GE Healthcare, USA) pre-equilibrated with HEPES buffer (50 mM HEPES, 100 mM NaCl; pH 7.4). Proteins were eluted using a NaCl gradient (100 mM to 1000 mM) at a flow rate of 1 mL/min using an AKTA Purifier fast protein liquid chromatography (FPLC) system (GE Healthcare, USA). The eluted fractions were collected using a Frac-950 fraction collector (GE Healthcare, USA), pooled, concentrated to 2 mL using a 30 kDa molecular weight cut-off centrifugal concentrator (Pall, USA), and desalted using a HiTrap Desalting 5 mL column (GE Healthcare, USA) at a flow rate of 2 mL/min via the FPLC system. The desalted proteins in HEPES buffer were subsequently concentrated to 2 mL using a 30 kDa molecular weight cut-off centrifugal concentrator (Pall, USA) and analysed by SDS-PAGE and western blotting.

The CΔ116-M $\Delta$ NV-CP was purified with the immobilized metal affinity chromatography (IMAC) method as described previously (33). The clarified crude lysate was

applied to HisTrap HP 1 mL columns (GE Healthcare, USA) pre-equilibrated with HEPES buffer (25 mM HEPES, 500 mM NaCl; pH 7.4). Proteins were eluted in steps using HEPES buffer with increasing concentrations of imidazole (50 mM, 100 mM, 150 mM, 200 mM and 500 mM). Positive fractions were pooled, concentrated, desalted and analysed by SDS-PAGE and western blotting.

### Dynamic light scattering (DLS) analysis

Purified chimeric VLPs (20 µg/mL) were passed through a 0.22 µm-syringe filter and subsequently analysed with a Zetasizer Nano ZS (Malvern Panalytical, UK) to assess the particle size and homogeneity at a temperature of 24 °C.

### Scanning transmission electron microscopy (STEM)

Purified chimeric VLPs (0.25 to 0.30 mg/mL) were applied to 300-mesh copper grids, and negatively stained with 2% (w/v) uranyl acetate for 8 minutes. After air-drying the grids, they were examined under a Hitachi H7700 transmission electron microscope (TEM, Hitachi, Tokyo, Japan) to assess the morphology and size of the VLPs.

### Antigenicity assay

The purified CΔ116-M $\Delta$ NV-CP<sup>RBD</sup> was diluted in HEPES buffer to concentrations ranging from 0.2 to 100 µg/mL. A 96-well microtiter plate was coated with 100 µL of each diluted samples, with HEPES buffer serving as the negative control. SARS-CoV-2 RBD, which produced and purified in a previous study (34), was used as the positive control. After incubation with an anti-SARS-CoV-2 RBD monoclonal antibody, the wells were treated with an anti-mouse alkaline phosphatase-conjugated antibody (1:5000 dilution in TBS buffer; KPL, USA; 100 µL). Colour development was initiated by adding p-nitrophenyl phosphate (p-NPP) substrate (100 µL), and absorbance was measured at 405 nm using an ELx800 microtiter plate reader (Bio-Tek Instruments, Winooski, VT, USA).

### Immunisation of BALB/c mice

Animal studies were approved by the Institutional Animal Care and Use Committee (IACUC), Universiti Putra Malaysia (R024/2021). Female BALB/c mice (n=8 per group), aged about 5–6 weeks, were acclimatized for 6 weeks to reach maturity. At week 7, the mice were immunised subcutaneously with purified chimeric VLPs (0.34 mg/mL; 100 µL), HEPES buffer and purified VLPs derived from CΔ116-M $\Delta$ NV-CP, with or without AddaVax (InvivoGen, USA) were included as controls. Two boosters were given at 3-week intervals. Blood samples were collected via submandibular bleeding before each injection and 1 week after the second booster. Serum was obtained following 30 minutes of room temperature incubation and subsequent centrifugation at 3500 x g for 10 minutes at 25°C, then stored at -80°C until further use.

### Immunogenicity analysis of chimeric VLPs

Purified SARS-CoV-2 RBD (2 µg/mL; 100 µL) was coated onto a microtiter plate and incubated with diluted mouse sera (1:2000 dilution). Detection was performed using anti-mouse alkaline phosphatase-conjugated antibody (1:5000 dilution in TBS buffer; KPL, USA; 100 µL), and the reaction was developed with p-nitrophenyl phosphate (p-NPP; 100 µL). Absorbance at wavelength 405 nm ( $A_{405}$ ) was measured using a ELx800 microtiter plate reader (Bio-Tek Instruments, Winooski, VT, USA).

### Immunophenotyping of mouse splenocytes

At week 14, the mice spleens were harvested and processed as follows: spleen were meshed through a cell strainer (70 µm; BD Biosciences, USA) in 1 mL phosphate buffered saline (PBS) buffer (137 mM NaCl, 10 mM  $\text{Na}_2\text{HPO}_4$ , 2.7 mM KCl, 1.5 mM  $\text{KH}_2\text{PO}_4$ ; pH 7.4). The resulting suspension was centrifuged at 300 x g for 10 minutes at 4°C. Cell pellets were resuspended in 10 mL erythrocyte lysis buffer (155 mM  $\text{NH}_4\text{Cl}$ , 10 mM  $\text{KHCO}_3$ , 0.1 mM EDTA; pH 7.4) and incubated at 4°C for 10 minutes. After centrifugation at 300 x g for 10 minutes, the pellets were washed twice, resuspended in 1 mL PBS buffer, and cell counts were performed using a haemocytometer. Cells were diluted to 2 million cells/mL, and 1 mL was aliquoted into each of three microcentrifuge tubes in duplicate. Two tubes were respectively introduced with 2 different sets of antibodies conjugated to fluorochromes: anti-CD3-APC, CD4-PE-Cy7 and CD8A-APC-H7; anti-F4/80-PE (BD Biosciences, USA) while the third tube served as a blank. The cell suspensions were incubated on ice in the dark for 2 hours and pelleted via centrifugation before fixing the cells in 1 mL PBS buffer containing 1% (w/v) paraformaldehyde at 4°C. After fixing for 24 hours, the cells were analysed with a flow cytometer, FACSCanto II (BD Biosciences, USA).

### Statistical analysis

The results of the immunogenicity assay, immunophenotyping of mouse splenocytes, and cytokine concentration in mouse sera were analysed using one-way analysis of variance (ANOVA), followed by Duncan's multiple range test to assess the significance of variations between different groups. Statistical analysis was conducted using IBM SPSS Statistics version 22 for Windows (IBM Corporation, Armonk, NY, USA). Results with p-value of <0.05 was determined as statistically significant, <0.001 as highly significant and <0.0001 as extremely significant.

### Ethical clearance

The study was conducted in accordance with the guidelines of the Declaration of Helsinki and approved by the Institutional Animal Care and Use Committee (IACUC), Universiti Putra Malaysia, with approval number R024/2021 for a duration from 2 July 2021 to 2 July 2022.

## RESULTS

### Construction of recombinant plasmid

During PCR amplification, the P-domain of *MrNV*-CP was deliberately excluded, resulting in the creation of truncated *MrNV*-CP variant, termed  $\text{C}\Delta 116$ -*MrNV*-CP. This modification facilitated the fusion and surface presentation of SARS-CoV-2 RBD. The coding sequences of  $\text{C}\Delta 116$ -*MrNV*-CP and SARS-CoV-2 RBD were cloned into the pTrcHis2-TOPO vector, forming the recombinant plasmid pTrcHis- $\text{C}\Delta 116$ -*MrNV*-CP<sup>RBD</sup> encoding the 478-residue recombinant protein  $\text{C}\Delta 116$ -*MrNV*-CP<sup>RBD</sup> (Figure 1a and 1b). Restriction enzyme digestion confirmed the successful construction of pTrcHis- $\text{C}\Delta 116$ -*MrNV*-CP<sup>RBD</sup>, as evidenced by distinct bands observed upon *EcoRI* and *HindIII* digestion (Figure 1c).

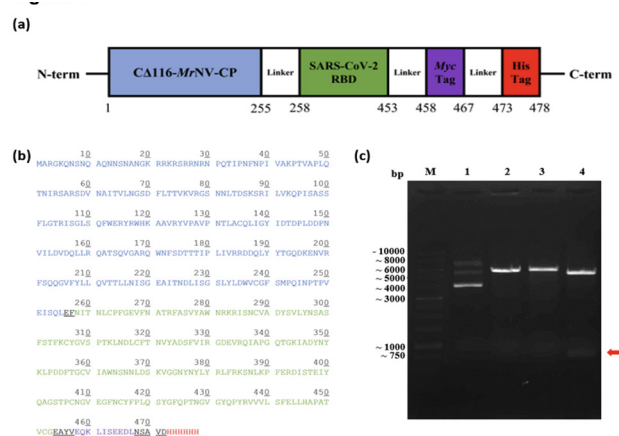


**Figure 1: Protein construct encoded by recombinant plasmid pTrcHis- $\text{C}\Delta 116$ -*MrNV*-CP<sup>RBD</sup>.** (a) Schematic representation of P-domain truncated-*MrNV*-CP fused with SARS-CoV-2 RBD ( $\text{C}\Delta 116$ -*MrNV*-CP<sup>RBD</sup>). The numbers indicate amino acid positions of  $\text{C}\Delta 116$ -*MrNV*-CP<sup>RBD</sup> (b) Primary amino acid sequences of  $\text{C}\Delta 116$ -*MrNV*-CP<sup>RBD</sup>. The amino acids sequence of P-domain truncated-*MrNV*-CP, SARS-CoV-2 RBD, myc-tag and His-tag are coloured in blue, green, purple and red respectively. Amino acid linkers are underlined. (c) Restriction enzyme digestion profile of recombinant plasmid pTrcHis- $\text{C}\Delta 116$ -*MrNV*-CP<sup>RBD</sup>. Lane M: 1 kb DNA ladder, Lane 1: Undigested plasmid (control), Lane 2: single digestion with *EcoRI*, Lane 3: single digestion with *HindIII*, Lane 4: double digestion with *EcoRI* and *HindIII*. Red arrow indicates a faint band of ~750 bp corresponding to the SARS-CoV-2 RBD insert.

### Expression and purification of recombinant proteins

The recombinant plasmid pTrcHis- $\text{C}\Delta 116$ -*MrNV*-CP<sup>RBD</sup> was introduced into *E. coli* BL21 (DE3) competent cells and protein expression was induced using 1 mM IPTG. After cell harvesting and lysis, the crude lysate was loaded onto a cation exchange column using FPLC, with protein elution achieved over a gradient of NaCl (Figure 2a). SDS-PAGE analysis (Figure 2b) showed that the  $\text{C}\Delta 116$ -*MrNV*-CP<sup>RBD</sup> was highly pure in fractions B11 and B10 (Lanes 6 and 7), appearing as a single protein band slightly above the 52 kDa protein marker, corresponding to the calculated molecular mass of  $\text{C}\Delta 116$ -*MrNV*-CP<sup>RBD</sup> at ~54.2 kDa. Other fractions (A5 to A7, Lanes 2 to 4) contained host proteins alongside

the target proteins, were therefore not used for further analysis. Fraction B11 was further analysed by SDS-PAGE (Figure 2c) and western blot (Figure 2d), with SARS-CoV-2 RBD serving as a positive control. The western blot analysis confirmed the identity of the target protein  $\Delta 116$ -MrNV-CP<sup>RBD</sup> at ~54 kDa in Lane 1, while the positive control SARS-CoV-2 RBD appeared at ~32 kDa in Lane 2. Notably, the yield of  $\Delta 116$ -MrNV-CP<sup>RBD</sup> from 1 L culture was approximately 0.2 mg, as determined using the Bradford assay.

The control recombinant protein  $\Delta 116$ -MrNV-CP was expressed under similar conditions, but purified using Immobilized Metal Affinity Chromatography (IMAC). SDS-PAGE analysis (Figure 2e) showed two bands at ~35 kDa in Lane 5, consistent with the calculated molecular mass of  $\Delta 116$ -MrNV-CP at ~32.7 kDa. Western blot validation (Figure 2f) using an anti-histidine monoclonal antibody confirmed the identity of  $\Delta 116$ -MrNV-CP, with the smaller band likely representing proteolytic degradation products at the N-terminus of MrNV-CP, as observed previously (26, 27, 35).

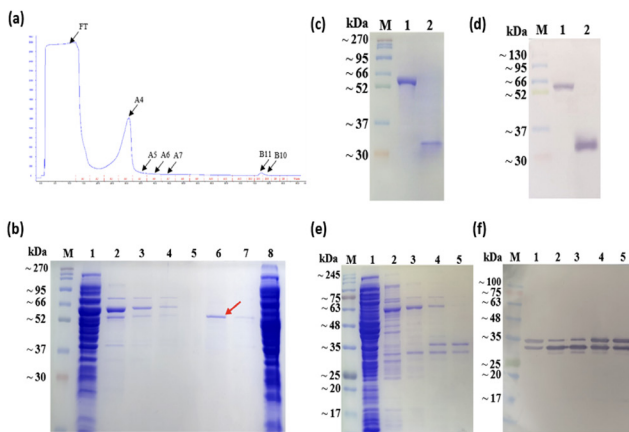


**Figure 2: Purification of chimeric proteins.** (a) FPLC chromatogram of  $\Delta 116$ -MrNV-CP<sup>RBD</sup> purified via cation exchange chromatography. The arrows indicate the fractions analysed using SDS-PAGE. (b) SDS-PAGE gel image of FPLC fractions. Lane M: protein ladder, lanes 1 to 4: fractions A4 – A7, lane 5: intentionally left empty, lanes 6 and 7: fractions B11 and B10, lane 8: sample injection flow through (FT). The target band is indicated by the red arrow. (c) SDS-PAGE gel image showing the protein ladder at Lane M, purified  $\Delta 116$ -MrNV-CP<sup>RBD</sup> in Lane 1 (~54 kDa) and purified SARS-CoV-2 RBD alone in Lane 2 (~32 kDa), followed by Western blot (d) probed with anti-SARS-CoV-2 RBD monoclonal antibody. (e) SDS-PAGE gel image of IMAC fractions of  $\Delta 116$ -MrNV-CP. Lane M: protein ladder, lanes 1 – 5: IMAC fractions of  $\Delta 116$ -MrNV-CP eluted with increasing concentrations of imidazole (50 mM to 500 mM). (f) Western blot probed with anti-histidine monoclonal antibody. The purified SARS-CoV-2 RBD was given as a gift by Dr Kiven Kumar (34).

### Structural characterization of recombinant proteins

The size and homogeneity of purified  $\Delta 116$ -MrNV-CP<sup>RBD</sup> were assessed by DLS and STEM. DLS measurements indicated an average particle size of ~19.49 nm with a polydispersity index of 0.466 (Figure 3a), while STEM images revealed spiky spherical particles measuring  $14 \pm 1$  nm in diameter (Figure 3b and 3c).

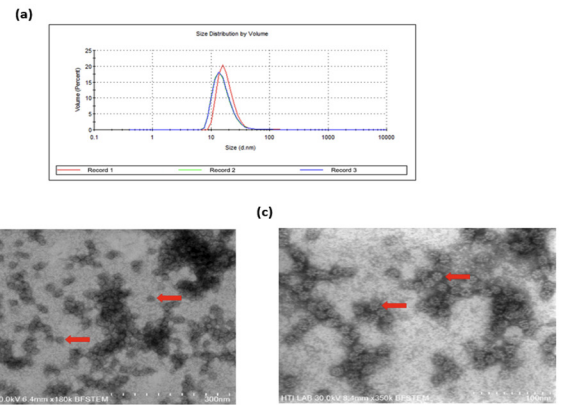


**Figure 3: Structural characterization of recombinant plasmid pTrcHis- $\Delta 116$ -MrNV-CP<sup>RBD</sup>.** (a) Size distribution graph of  $\Delta 116$ -MrNV-CP<sup>RBD</sup> measured by Zetasizer Nano ZS. The particles show an average particle size of ~19.49 nm with a polydispersity index of 0.466. Scanning transmission electron microscopic (STEM) analysis of  $\Delta 116$ -MrNV-CP<sup>RBD</sup> taken at 180,000 x (b) and 350,000 x (c) magnifications respectively. The particles (as indicated by the red arrow) exhibit a spiky outer shell.

### Antigenicity of the chimeric VLPs

An enzyme-linked immunosorbent assay (ELISA) was performed to analyse the antigenicity of  $\Delta 116$ -MrNV-CP<sup>RBD</sup>. The assay demonstrated concentration-dependent recognition of the SARS-CoV-2 RBD displayed on the VLPs by an anti-SARS-CoV-2 RBD monoclonal antibody (Figure 4). Importantly, the negative control,  $\Delta 116$ -MrNV-CP, did not exhibit binding to the antibody, confirming the specificity of antigen presentation on the chimeric VLPs.

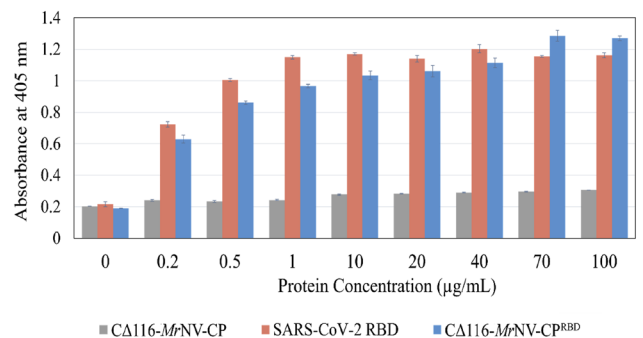


**Figure 4: Antigenicity of recombinant proteins at different protein concentrations.** The level of anti-SARS-CoV-2 RBD monoclonal antibodies bound to the RBD displayed on the VLPs formed by  $\Delta 116$ -MrNV-CP<sup>RBD</sup> increases proportionally to the protein concentrations, same as the positive control SARS-CoV-2 RBD protein. The error bars represent the standard deviation (SD). The experiment was completed in triplicates.

### Immunogenicity assessment of chimeric VLPs in BALB/c mice

BALB/c mice were immunized with  $\Delta 116$ -MrNV-CP<sup>RBD</sup> formulated with AddaVax, showing detectable specific antibody responses against SARS-CoV-2 three weeks after the first injection at week 10 (Figure 5). Subsequent booster injections (first booster, week 13;

second booster, week 14) further elevated antibody titres, particularly in the presence of the adjuvant, demonstrating robust immune responses. Interestingly, the non-adjuvanted formulation also induced specific antibody production against SARS-CoV-2 RBD in week 14, albeit at lower levels compared to the adjuvanted group. Control groups injected with HEPES buffer or  $\Delta$ 116-*M* $\Delta$ NV-CP, regardless the presence of adjuvant, did not show specific antibody production throughout the study.

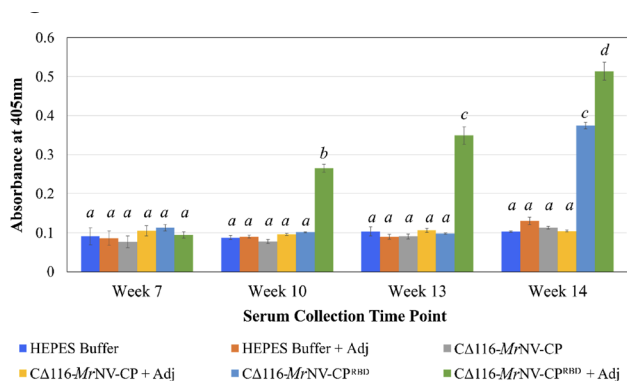


**Figure 5: Immunogenicity of the chimeric virus-like particles in BALB/c mice.** Level of antibody against the RBD of SARS-CoV-2 in serum of BALB/c mice collected during immunisation. Serum samples were collected in week 7 (before immunisation), week 10 (after primary injection), week 13 (after first booster) and week 14 (after second booster) through submandibular bleeding. Two out of six analytes, which are  $\Delta$ 116-*M* $\Delta$ NV-CP<sup>RBD</sup> with or without adjuvant were able to elicit antibody production in BALB/c mice against SARS-CoV-2 RBD.  $\Delta$ 116-*M* $\Delta$ NV-CP<sup>RBD</sup> with adjuvant demonstrated higher antibody titre as compared to  $\Delta$ 116-*M* $\Delta$ NV-CP<sup>RBD</sup> without adjuvant. The alphabets (*a, b, c, d*) on top of each bar represent the statistical significance ( $P < 0.0001$ ) of result between each group. The experiment was completed in triplicates.

### Immunophenotyping of mouse splenocytes

Flow cytometric analysis of splenocytes from immunized mice revealed distinct immunological profiles. As shown in Figure 6A, the ratio of cytotoxic T-cells (CTL) to helper T-cells (Th) (CD8+/CD4+) population was highest in the mice injected with  $\Delta$ 116-*M* $\Delta$ NV-CP in the presence of adjuvant, followed by  $\Delta$ 116-*M* $\Delta$ NV-CP<sup>RBD</sup> with and without adjuvant. The mice injected with HEPES buffer with adjuvant and  $\Delta$ 116-*M* $\Delta$ NV-CP without adjuvant had a similar ratio of approximately 0.2, while the HEPES buffer alone showed the lowest ratio, lesser than 0.1, indicating a significantly lower CTL population relative to Th cells.

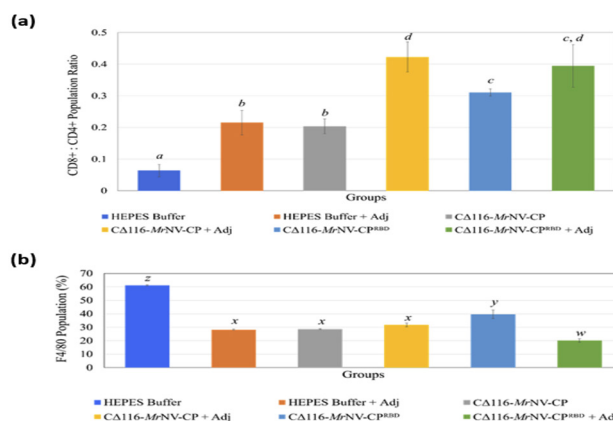


**Figure 6: Immunophenotyping of BALB/c mice spleen harvested at week 14 of immunisation.** (a) CD8+:CD4+ population ratio. The alphabets (*a, b, c, d*) on top of each bar represent the statistical significance ( $P < 0.05$ ) of result between each group. (b) F4/80 population. The alphabets (*w, x, y, z*) on top of each bar represent the statistical significance ( $P < 0.01$ ) of result between each group. The gating strategy and the representative scatter plots are shown in Supplementary materials Figure S1-S3.

With respect to macrophage population, the mice injected with HEPES buffer without adjuvant had the highest macrophage levels (61.1%), followed by those injected with  $\Delta$ 116-*M* $\Delta$ NV-CP<sup>RBD</sup> without adjuvant (39.6%) (Figure 6B). The mice received HEPES buffer with adjuvant and  $\Delta$ 116-*M* $\Delta$ NV-CP with or without adjuvant exhibited similar macrophage levels at approximately 30%, while  $\Delta$ 116-*M* $\Delta$ NV-CP<sup>RBD</sup> with adjuvant group had the lowest (20.2%). These findings suggest that  $\Delta$ 116-*M* $\Delta$ NV-CP<sup>RBD</sup>, with or without adjuvant, can elicit both cellular and humoral immune responses in BALB/c mice.

### DISCUSSION

Since Covid-19 was declared a pandemic in March 2020, several vaccines based on mRNA technology, inactivated whole virus, protein subunits, and adenoviral vectors have been approved for emergency use. However, concerns remain about the safety and efficacy of these vaccines in preventing SARS-CoV-2 infections. Additionally, the high cost and advanced technology required for the production and storage of these vaccines have hindered global vaccination efforts, particularly in low-income countries. Therefore, there is an urgent need to develop a vaccine that is safe, effective, and

affordable for the prevention of SARS-CoV-2 infection.

VLPs offer a promising platform for vaccine development, as they mimic the structure of viruses but lack genetic material, making them non-infectious while still eliciting strong immune responses. By displaying foreign epitopes, such as the SARS-CoV-2 receptor-binding domain (RBD), on VLPs, the immune system can be effectively stimulated, leading to higher antibody production. In this study, the SARS-CoV-2 RBD was fused to a C-terminally truncated version of *MnNV*-CP, generating the recombinant protein  $\Delta 116$ -*MnNV*-CP<sup>RBD</sup>. Upon VLP formation, the RBD was successfully displayed on the surface of the particles.

The recombinant protein  $\Delta 116$ -*MnNV*-CP<sup>RBD</sup> was produced by introducing a plasmid encoding the P-domain truncated *MnNV*-CP fused to the SARS-CoV-2 RBD into *E. coli* BL21 (DE3) cells (Figure 1). Protein expression was induced by IPTG, and the recombinant protein was purified using a cation exchange column connected to a FPLC system. This method offers several advantages, including faster purification, higher resolution, and reduced human intervention, leading to consistent results. HEPES buffer with a NaCl gradient (100 to 1000 mM) was used to elute the recombinant protein from the column. SDS-PAGE analysis revealed that pure  $\Delta 116$ -*MnNV*-CP<sup>RBD</sup> was eluted at 1 M NaCl, although some host proteins were co-eluted at lower NaCl concentrations, likely due to surface charge differences. The fractions containing  $\Delta 116$ -*MnNV*-CP<sup>RBD</sup> (Figure 2a and b; fractions B11 and B10) were pooled and subsequently probed with anti-RBD monoclonal using western blot. The FPLC-purified  $\Delta 116$ -*MnNV*-CP<sup>RBD</sup> yielded ~0.2 mg/L, as determined using the Bradford assay. Protein purity was estimated to be ~90% as verified by SDS-PAGE and western blot. The selection of cation exchange chromatography, tailored to the protein's positive net charge, effectively minimized contaminants, yielding high purity and facilitating reproducibility across batches in alignment with established VLPs purification methods. The approach is consistent with previous studies. One study reported a yield of ~2.4mg/L for NvC-aD (Hepatitis B 'a' determinant) expressed using a similar fusion strategy of *MnNV*-CP with immunogenic epitopes (30). Another study found that *E. coli* expressed *MnNV*-CP alone yielded ~1.5mg/mL, with an estimated cost production cost of 15 USD/mg and a production time of 3 days (27).

The size and morphology of the VLPs formed by  $\Delta 116$ -*MnNV*-CP<sup>RBD</sup> were analyzed using DLS and STEM. DLS analysis indicated an average particle size of ~19.5 nm (Figure 3a), while STEM revealed spiky spherical particles measuring approximately  $14 \pm 1$  nm (Figure 3b). The difference between these measurements is attributed to the different states of the VLPs during analysis: DLS measures hydrated particles, which include the

hydration shell, resulting in a larger apparent diameter, whereas STEM measures dehydrated particles, leading to a smaller size (36, 37). This discrepancy is consistent with previous studies (29, 30), and it highlights the importance of considering measurement conditions when interpreting particle size data. The PDI of 0.466 indicates some heterogeneity, which could indicate the presence of various particle sizes due to fusion of SARS-CoV-2 RBD, aligning with TEM observation.

Previous study have shown that the full-length *MnNV* capsid protein forms VLPs of about 30 nm in diameter, observed via TEM (26). Short peptides (12-29 amino acids) fusions to *MnNV*-CP C-terminus yielded similar-sized chimeric VLPs (32, 33, 38), whereas larger peptide such as the 133-residue domain III of Japanese Encephalitis Virus (JEV) envelope protein, reduce VLP size to ~18 nm (29). In this study, the recombinant protein  $\Delta 116$ -*MnNV*-CP<sup>RBD</sup> displaying the 196-residue SARS-CoV-2 RBD, was shown to self-assemble into VLPs, forming spiky spheric particles of approximately  $14 \pm 1$  nm in STEM images. Contrasting with the VLPs formed by P-domain truncated-*MnNV*-CP ( $\Delta 116$ -*MnNV*-CP), which lack foreign epitopes and measured around 19 nm (35), it is hypothesised that larger peptide fusions may lead to  $T=1$  symmetry, differing from  $T=3$  icosahedral symmetry in full-length *MnNV*-CP and native virions (25, 29). Further investigation is needed to verify these findings' impact on VLP stability, immunogenicity, or other properties.

ELISA was performed to assess the antigenicity of the chimeric VLPs (Figure 4). The results demonstrated that the RBD displayed on the VLPs was specifically recognized by anti-SARS-CoV-2 RBD monoclonal antibodies, confirming that the antigen was properly presented on the surface of the VLPs. This antigenic display is crucial for triggering immune responses when the vaccine is administered to a host. Similar results were obtained when the RBD was derived from VOCs  $\beta$ - and  $\delta$ -strains (34).

The immunogenicity of the  $\Delta 116$ -*MnNV*-CP<sup>RBD</sup> VLPs was evaluated in BALB/c mice. The mice were immunized with the VLPs, both with and without the adjuvant AddaVax, and their antibody responses were monitored. The results showed that mice immunized with the adjuvanted VLPs produced significantly higher antibody titres against SARS-CoV-2 RBD compared to those immunized without adjuvant (Figure 5). This suggests that AddaVax enhances the immunogenicity of the VLPs, potentially reducing the number of booster doses required to achieve protective immunity (29).

In addition to humoral responses, cellular immune responses were assessed by immunophenotyping splenocytes from immunized mice (Figure 6). Flow cytometry analysis revealed a higher CD8<sup>+</sup>/CD4<sup>+</sup> T-cell ratio in mice immunized with adjuvanted VLPs,

indicating a more balanced immune response. The presence of a balanced CD8+ T-cell population is important for providing protection against intracellular pathogens like viruses (39). Interestingly, the adjuvanted CΔ116-*M*rNV-CP displayed greater immune responses than the adjuvanted CΔ116-*M*rNV-CP<sup>RBD</sup>, a finding that was unexpected. Additionally, macrophage populations analysis revealed significantly higher levels in mice immunized with HEPES buffer alone compared to other groups. These unusual observations may be due to mild inflammation resulting from external factors, such as minor injuries among the mice, or variations in experimental conditions. To better elucidate these dynamics, further functional assays or histological evaluation are recommended.

Macrophage populations were also analyzed, revealing that mice immunized with HEPES buffer alone had significantly higher macrophage levels compared to other groups. This increase may be due to mild inflammation caused by external factors, such as minor injuries among the mice, or variations in experimental conditions.

## CONCLUSION

This study successfully produced CΔ116-*M*rNV-CP, a versatile VLP platform capable of presenting large foreign epitopes and eliciting both cellular and humoral responses in BALB/c mice. SARS-CoV-2 RBD was chosen as the epitope due to its immunogenic properties, while P-domain truncated-*M*rNV-CP was selected for its ability to self-assemble into VLPs and effectively display large foreign epitopes. The fusion of both proteins formed the recombinant protein CΔ116-*M*rNV-CP<sup>RBD</sup>, which was purified using cation exchange chromatography, requiring HEPES buffer containing 1 M NaCl for optimal purity. The diameter of the chimeric VLPs, measured by DLS was ~5 nm larger than that observed using STEM (~ 14 nm), due to the varying states of the VLPs during measurement. Importantly, the SARS-CoV-2 RBD displayed on the chimeric VLPs was antigenic, and when adjuvanted with AddaVax, induced specific antibodies in immunized mice, demonstrating its potential as a candidate for a Covid-19 VLP-based vaccine.

## ACKNOWLEDGEMENT

This work was funded by Universiti Putra Malaysia (Grant number: UPM/800-3/3/1/GPB/2019/9671400).

## REFERENCES

1. WHO Covid-19 dashboard [Internet]. 2024. Available from: <https://data.who.int/dashboards/Covid19/cases>.
2. Lefkowitz EJ, Dempsey DM, Hendrickson RC, Orton RJ, Siddell SG, Smith DB. Virus taxonomy: the database of the International Committee on Taxonomy of Viruses (ICTV). *Nucleic Acids Res.* 2018;46(D1):D708-D17.10.1093/nar/gkx932.
3. Chen Y, Guo D. Molecular mechanisms of coronavirus RNA capping and methylation. *Virol Sin.* 2016;31(1):3-11.10.1007/s12250-016-3726-4.
4. Ge XY, Li JL, Yang XL, Chmura AA, Zhu G, Epstein JH, et al. Isolation and characterization of a bat SARS-like coronavirus that uses the ACE2 receptor. *Nature.* 2013;503(7477):535-8.10.1038/nature12711.
5. Wang LF, Shi Z, Zhang S, Field H, Daszak P, Eaton BT. Review of bats and SARS. *Emerg Infect Dis.* 2006;12(12):1834-40.10.3201/eid1212.060401.
6. Khan S, Liu J, Xue M. Transmission of SARS-CoV-2, Required Developments in Research and Associated Public Health Concerns. *Front Med (Lausanne).* 2020;7:310.10.3389/fmed.2020.00310.
7. Mirtaleb MS, Falak R, Heshmatnia J, Bakhshandeh B, Taheri RA, Soleimanjahi H, et al. An insight overview on Covid-19 mRNA vaccines: Advantageous, pharmacology, mechanism of action, and prospective considerations. *Int Immunopharmacol.* 2023;117:109934.10.1016/j.intimp.2023.109934.
8. Huang C, Wang Y, Li X, Ren L, Zhao J, Hu Y, et al. Clinical features of patients infected with 2019 novel coronavirus in Wuhan, China. *Lancet.* 2020;395(10223):497-506.10.1016/S0140-6736(20)30183-5.
9. Rehman MFU, Fariha C, Anwar A, Shahzad N, Ahmad M, Mukhtar S, et al. Novel coronavirus disease (Covid-19) pandemic: A recent mini review. *Comput Struct Biotechnol J.* 2021;19:612-23.10.1016/j.csbj.2020.12.033.
10. Letko M, Marzi A, Munster V. Functional assessment of cell entry and receptor usage for SARS-CoV-2 and other lineage B betacoronaviruses. *Nat Microbiol.* 2020;5(4):562-9.10.1038/s41564-020-0688-y.
11. Lan J, Ge J, Yu J, Shan S, Zhou H, Fan S, et al. Structure of the SARS-CoV-2 spike receptor-binding domain bound to the ACE2 receptor. *Nature.* 2020;581(7807):215-20.10.1038/s41586-020-2180-5.
12. Hoffmann M, Kleine-Weber H, Schroeder S, Kruger N, Herrler T, Erichsen S, et al. SARS-CoV-2 Cell Entry Depends on ACE2 and TMPRSS2 and Is Blocked by a Clinically Proven Protease Inhibitor. *Cell.* 2020;181(2):271-80 e8.10.1016/j.cell.2020.02.052.
13. Safa O, Hassani-Azad M, Farashahinejad M, Davoodian P, Dadvand H, Hassanipour S, et al. Effects of Licorice on clinical symptoms and laboratory signs in moderately ill patients with pneumonia from Covid-19: A structured summary of a study protocol for a randomized controlled trial. *Trials.* 2020;21(1):790.10.1186/s13063-020-04706-3.

14. Sivaraman H, Er SY, Choong YK, Gavor E, Sivaraman J. Structural Basis of SARS-CoV-2- and SARS-CoV-Receptor Binding and Small-Molecule Blockers as Potential Therapeutics. *Annu Rev Pharmacol Toxicol.* 2021;61:465-93.10.1146/annurev-pharmtox-061220-093932.
15. Ying T, Li H, Lu L, Dimitrov DS, Jiang S. Development of human neutralizing monoclonal antibodies for prevention and therapy of MERS-CoV infections. *Microbes Infect.* 2015;17(2):142-8.10.1016/j.micinf.2014.11.008.
16. Polack FP, Thomas SJ, Kitchin N, Absalon J, Gurtman A, Lockhart S, et al. Safety and Efficacy of the BNT162b2 mRNA Covid-19 Vaccine. *N Engl J Med.* 2020;383(27):2603-15.10.1056/NEJMoa2034577.
17. Baden LR, El Sahly HM, Essink B, Follmann D, Neuzil KM, August A, et al. Phase 3 Trial of mRNA-1273 during the Delta-Variant Surge. *N Engl J Med.* 2021;385(26):2485-7.10.1056/NEJMc2115597.
18. Knoll MD, Wonodi C. Oxford-Astra Zeneca Covid-19 vaccine efficacy. *Lancet.* 2021;397(10269):72-4.10.1016/S0140-6736(20)32623-4.
19. Gao Q, Bao L, Mao H, Wang L, Xu K, Yang M, et al. Development of an inactivated vaccine candidate for SARS-CoV-2. *Science.* 2020;369(6499):77-81.10.1126/science.abc1932.
20. Rauch S, Jasny E, Schmidt KE, Petsch B. New Vaccine Technologies to Combat Outbreak Situations. *Front Immunol.* 2018;9:1963.10.3389/fimmu.2018.01963.
21. Mohsen MO, Zha L, Cabral-Miranda G, Bachmann MF. Major findings and recent advances in virus-like particle (VLP)-based vaccines. *Semin Immunol.* 2017;34:123-32.10.1016/j.smim.2017.08.014.
22. Ura T, Okuda K, Shimada M. Developments in Viral Vector-Based Vaccines. *Vaccines (Basel).* 2014;2(3):624-41.10.3390/vaccines2030624.
23. Arcier JM, Herman F, Lightner DV, Redman RM, Mari J, Bonami JR. A viral disease associated with mortalities in hatchery-reared postlarvae of the giant freshwater prawn *Macrobrachium rosenbergii*. *Dis. Aquat. Organ.* 1999;38:177-81. DOI: 10.3354/dao038177.
24. Ho KL, Gabrielsen M, Beh PL, Kueh CL, Thong QX, Streetley J, et al. Structure of the *Macrobrachium rosenbergii* nodavirus: A new genus within the Nodaviridae? *PLoS Biol.* 2018;16(10):e3000038.10.1371/journal.pbio.3000038.
25. Ho KL, Kueh CL, Beh PL, Tan WS, Bhella D. Cryo-Electron Microscopy Structure of the *Macrobrachium rosenbergii* Nodavirus Capsid at 7 Angstroms Resolution. *Sci Rep.* 2017;7(1):2083.10.1038/s41598-017-02292-0.
26. Goh ZH, Tan SG, Bhassu S, Tan WS. Virus-like particles of *Macrobrachium rosenbergii* nodavirus produced in bacteria. *J Virol Methods.* 2011;175(1):74-9.10.1016/j.jviromet.2011.04.021.
27. Kueh CL, Yong CY, Masoomi Dezfooli S, Bhassu S, Tan SG, Tan WS. Virus-like particle of *Macrobrachium rosenbergii* nodavirus produced in *Spodoptera frugiperda* (Sf9) cells is distinctive from that produced in *Escherichia coli*. *Biotechnol Prog.* 2017;33(2):549-57.10.1002/btpr.2409.
28. Jariyapong P, Chotwiwatthanakun C, Somrit M, Jitrapakdee S, Xing L, Cheng HR, et al. Encapsulation and delivery of plasmid DNA by virus-like nanoparticles engineered from *Macrobrachium rosenbergii* nodavirus. *Virus Res.* 2014;179:140-6.10.1016/j.virusres.2013.10.021.
29. Kumar K, Ong HK, Tan WS, Arshad SS, Ho KL. Immunological Analysis of Nodavirus Capsid Displaying the Domain III of Japanese Encephalitis Virus Envelope Protein. *Pharmaceutics.* 2021;13(11).10.3390/pharmaceutics13111826.
30. Ninyio NN, Ho KL, Ong HK, Yong CY, Chee HY, Hamid M, et al. Immunological Analysis of the Hepatitis B Virus "a" Determinant Displayed on Chimeric Virus-Like Particles of *Macrobrachium rosenbergii* Nodavirus Capsid Protein Produced in Sf9 Cells. *Vaccines (Basel).* 2020;8(2).10.3390/vaccines8020275.
31. Ong HK, Yong CY, Tan WS, Yeap SK, Omar AR, Razak MA, et al. An Influenza A Vaccine Based on the Extracellular Domain of Matrix 2 Protein Protects BALB/C Mice Against H1N1 and H3N2. *Vaccines (Basel).* 2019;7(3).10.3390/vaccines7030091.
32. Yong CY, Yeap SK, Goh ZH, Ho KL, Omar AR, Tan WS. Induction of humoral and cell-mediated immune responses by hepatitis B virus epitope displayed on the virus-like particles of prawn nodavirus. *Appl Environ Microbiol.* 2015;81(3):882-9.10.1128/AEM.03695-14.
33. Yong CY, Yeap SK, Ho KL, Omar AR, Tan WS. Potential recombinant vaccine against influenza A virus based on M2e displayed on nodaviral capsid nanoparticles. *Int J Nanomedicine.* 2015;10:2751-63.10.2147/IJN.S77405.
34. Kumar K, Tan WS, Arshad SS, Ho KL. Virus-like Particles of Nodavirus Displaying the Receptor Binding Domain of SARS-CoV-2 Spike Protein: A Potential VLP-Based Covid-19 Vaccine. *Int J Mol Sci.* 2023;24(5).10.3390/ijms24054398.
35. Ganesan H, Ho KL, Mariatulqabiah AR, Yong CY, Wong CL, Goh ZH, et al. Virus-like particles of *Macrobrachium rosenbergii* nodavirus: Particle size and capsid protein assembly domain. *Aquaculture.* 2022;561:738670.10.1016/j.aquaculture.2022.738670.
36. Laage D, Elsaesser T, Hynes JT. Water Dynamics in the Hydration Shells of Biomolecules. *Chem Rev.* 2017;117(16):10694-725.10.1021/acs.chemrev.6b00765.
37. Moryn MC. Protein hydration shell formation:

- Dynamics of water in biological systems exhibiting nanoscopic cavities. *J. Mol. Liq.* 2021;337:116584.10.1016/j.molliq.2021.116584.
38. Grataitong K, Huault S, Chotwiwatthanakun C, Jariyapong P, Thongsum O, Chawiwithaya C, et al. Chimeric virus-like particles (VLPs) designed from shrimp nodavirus (*MNV*) capsid protein specifically target EGFR-positive human colorectal cancer cells. *Sci Rep.* 2021;11(1):16579.10.1038/s41598-021-95891-x.
39. Sud D, Bigbee C, Flynn JL, Kirschner DE. Contribution of CD8+ T cells to control of *Mycobacterium tuberculosis* infection. *J Immunol.* 2006;176(7):4296-314.10.4049/jimmunol.176.7.4296.